Int J Adv Manuf Technol (2017) 90:3275–3288
DOI 10.1007/s00170-016-9628-7

ORIGINAL ARTICLE

Probabilistic high cycle fatigue behavior prediction of A356-T6 alloy considering the SDAS dispersion

A. Ben Ahmed[1] · **A. Nasr**[2] · **R. Fathallah**[1]

Received: 9 July 2016 / Accepted: 17 October 2016 / Published online: 4 November 2016

Abstract This paper proposes an engineering approach to determine the probabilistic Kitagawa diagram of defective A356-T6 aluminum alloy considering the modification introduced by varying the secondary dendrite arming spacing (SDAS). The developed approach is carried out by coupling of FE analysis, defect stress gradient (DSG) criterion, and Monte Carlo simulation (MCS) method. In this context, a 3D-finite element analysis (FEA) for different cases of defect sizes and loading conditions using ABAQUS commercial software is established. The nonlinear isotropic/kinematic hardening model implemented in ABAQUS is used to characterize material behavior. Comparing with experimental results, the developed probabilistic approach presents an efficient numerical tool for predicting fatigue limit under fully reserved tension and torsion loadings due to the random distribution of the SDAS parameter. These probabilistic Kitagawa diagrams allow the engineer to be engaged in a practical problem to evaluate the fatigue limit in a more efficient and safe way. In addition, the sensitivity effects of defect size and SDAS parameter for predicting fatigue limit of A356-T6 aluminum alloy under alternate tension and torsion loadings is discussed using response surface methodology (RSM).

Keywords Fatigue limit · Finite element analysis · Monte Carlo simulation · RSM · Probability density function PDF · SDAS

Nomenclature

A	Elongation to failure [mm]
E	Modulus of elasticity [MPa]
ϑ	Poisson's ratio
$f_{\{X\}}(\{X_i\})$	Joint probability density function
$f_{X_i}(x_i)$	Probability density function of the element x_i
$I(\{x\})$	Indicator failure function
L	Load function
N	Number of random sampling in the MCS
MCS	Monte Carlo simulation
P_f	Failure probability
RSM	Response surface methodology
S	Strength function
$\sqrt{J_{2,a}}$	Amplitude of the second invariant of the stress tensor [MPa]
R_σ	Load ratio
R_m	Ultimate tensile stress [MPa]
α and β	Material constants in Crossland criterion
P_f	Probability of failure
σ_D	Fatigue limit [MPa]
σ_a	Applied load [MPa]
σ_{-1}	Defect-free fatigue limit under fully reserved tension loading [MPa]
τ_{-1}	Defect-free fatigue limit under fully reserved torsion loading [MPa]
$R_{p0.2\%}$	Yield stress [MPa]
SDAS	Secondary dendrite arming spacing
HCF	High cycle fatigue
DSG	Defect stress gradient

✉ A. Ben Ahmed
amalbenahmed@gmail.com

[1] Laboratoire de Mécanique de Sousse (LMS), Ecole Nationale d'Ingénieurs de Sousse (ENISo), Université de Sousse, BP 264, Cité Erriadh, 4023 Sousse, Tunisia

[2] Laboratoire de Génie Mécanique (LGM), Institut préparatoire aux études d'ingénieurs de Monastir (IPEM), Université de Monastir, Avenue Ibn Eljazzar, 5019 Monastir, Tunisia

R	Defect radius
G_H	Stress gradient
$\overline{\overline{S}}$	Deviatoric stress tensor
$\sqrt{\text{area}}$	Murakami parameter [um]
REV	Representative elementary volume

1 Introduction

Aluminum alloy casting is widely employed in automotive and aerospace applications due to their high mechanical performances and dimensional stability. In most studies [1–10], it has been shown that fatigue behavior of A356-T6 is mainly affected by microstructure characterized by secondary dendrite arming spacing (SDAS) and casting defects such as shrinkage cavities, gas pores, notches, and oxide films. Several studies [1, 2, 9–14] have proved that surface porosity is the principle site of crack initiation in A356-T6 alloy.

In this context, many experimental investigations [1–6, 10, 13–18] have been made to determine the detrimental factors on fatigue resistance of A356-T6 alloy. As reported in [2, 10, 18], for porosity-free alloy, fatigue life is governed by SDAS and, for defective alloy, it is governed by both defect size (characterized by Murakami parameter $\sqrt{\text{area}}$ [19]) and SDAS. H.R. Ammar et al. [2] showed that, for A356-T6 material containing various casting defects, 92 % of the experimental samples were ruptured from surface pores, and they observed that the endurance limit decreases as the porosity density increases. Later, based on wide experimental investigations, Iben Houriya and Roy [18, 20, 21] observed that the SDAS has the main role in the formation of plastic strain and crack initiation when defect size is under 400 ∓ 100 μm. Besides, they showed that for coarser microstructure (high SDAS values), low fatigue limits are obtained and vice versa.

Porosity in cast aluminum material cannot be avoided for many reasons such as difficulties in controlling processing conditions, alloy quality, and the cooling rate level. Therefore, many researches [18, 20–23] have been carried out to determine the fatigue response of defective aluminum alloys. Based on experimental observations, Koutiri et al. [22] have shown that the fatigue life behavior of cast hypo-eutectic Al-Si alloy under multiaxial fatigue loading could not be predicted by the Dang Van criterion or any approach which could be written as a linear combination of the hydrostatic stress and the second invariant of the stress deviator tensor.

Later, Roy et al. [21] have made a comparative study to describe fatigue behavior of A356-T6 Using four approaches: (i) The Murakami relationship [19], (ii) linear elastic fracture mechanics [24], (iii) the critical distance method (CDM) [25], and (iiii) defect stress gradient criterion (DSG) [26]. They concluded that both the CDM and the DSG approaches are the most close to the experimental results for predicting fatigue limit under multiaxial load conditions. Recently, Iben Houriya et al. [18] have modified the DSG criterion by introducing a parameter that takes into account the microstructure effect. Comparing with experimental results, they demonstrated that the improved DSG criterion could describe adequately the fatigue behavior under multiaxial loading of A356-T6 alloy containing artificial and natural defects.

However, it should be noted that the previous HCF criteria proposed to determine the fatigue response of defective A356-T6 alloy are deterministic. Their applications use generally experimental endurance limits with failure probability equal to 50 %. In this case, they did not take into account the stochastic effects, particularly material dispersions introduced by varying the secondary dendrite arming spacing (SDAS).

The aim of this work is to develop a probabilistic approach to predict the high cycle fatigue (HCF) reliability of A356-T6 alloy. The proposed approach is released by coupling finite element analysis (FE) and the Monte Carlo reliability method. Therefore, a 3D FE analysis model containing a spherical defect is proposed to represent the porous material. Numerical simulations are carried out for different loadings and pore sizes using the nonlinear isotropic/kinematic hardening model. The random initial SDAS value distribution into the material produces a scatter of the representative loading point. All the results obtained for fully reserved tension and torsion loadings are in good agreement with experimental investigations. Moreover, the surface response method is chosen to characterize the correlation of SDAS and defect size and to determine the influence of these factors on the fatigue endurance limit.

2 Theoretical background

2.1 Defect stress gradient criterion (DSG)

In order to characterize the stress distribution around a defect and to quantify its impact on the fatigue limit under different loading conditions, Nadot et al. [27] proposed the defect stress gradient (DSG) criterion. They have found that only the hydrostatic part of the stress tensor affects the fatigue behavior. The proposed criterion is based on Crossland's formulation and it is defined as follows:

$$\sqrt{J_{2,a}} + \alpha P^*_{\max} \leq \beta \tag{1}$$

where

$$P^*_{\max} = P_{\max}\left(1 - a_d\left(\frac{G_H}{P_{\max}}\right)\right) \tag{2}$$

$J_{2,a}$ may be calculated as follows:

$$J_{2,a} = \frac{1}{2\sqrt{2}} \max_{t_i \in T} \left\{ \max_{t_i \in T} \sqrt{\left(\overline{\overline{S}}(t_i) - \overline{\overline{S}}(t_j)\right) : \left(\overline{\overline{S}}(t_i) - \overline{\overline{S}}(t_j)\right)} \right\} \quad (3)$$

where $\overline{\overline{S}}$ is the deviatoric stress tensor and G_H is the stress gradiant defined as

$$G_H = \left(P_{\max}(A) - P_{\max}\left(\sqrt{\text{area}}\right)\right) / \sqrt{\text{area}} \quad (4)$$

A is the most solicited point on the defect; $\sqrt{\text{area}}$ is the Murakami parameter; and a_d, α, and β are three coefficients experimentally identified.

The DSG criterion was improved later by Gadouini et al. [28] then by Vincent et al. [29] using Eshelby's method (Fig. 1) [24]. It is written now as

$$\sigma_{eq\nabla} = \sigma_{eq,max} - a \frac{\sigma_{eq,max} - \sigma_{eq,\infty}}{\sqrt{\text{area}}} \leq \beta \quad (5)$$

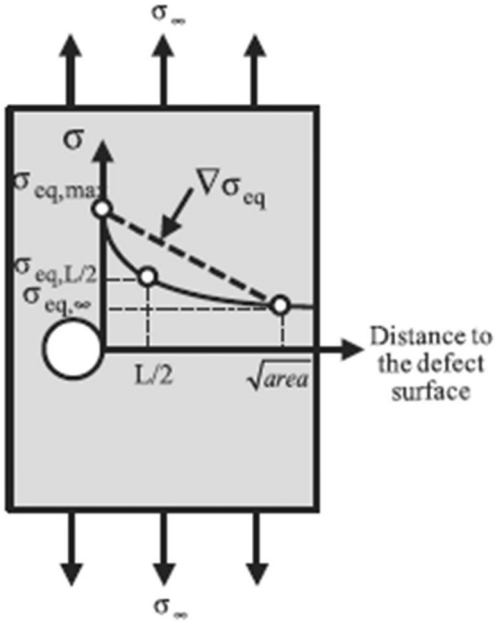

Fig. 1 Principle of DSG approach [24]

where $\sigma_{eq\nabla}$ is the equivalent stress given by the DSG criterion. $\sigma_{eq,max}$ and $\sigma_{eq,\infty}$ are the two equivalent stresses given by a multiaxial fatigue criterion in the most sollitated defect point and far from the defect, respectively.

Iben Houriya et al. [18] suggested modifying the DSG criterion with the introduction of the parameter λ_2 which designs the SDAS. They used the Crossland criterion to express the equivalent stress. According to their study, the DSG approach describing the fatigue behavior of A356-T6 alloy is given by the two following expressions:

(i) In the case of defect-free alloy, fatigue limit is only influenced by microstructure (SDAS) and it can be expressed as follows:

$$\sigma_{eq\nabla M} = \sigma_{Cr,mMax} = \beta_0 \exp\left(-\frac{\lambda_2}{\lambda_0}\right) \quad (6)$$

(ii) In the case of defective alloy, fatigue limit is influenced by both SDAS and defect size and it can be expressed as follows:

$$\sigma_{eq\nabla M} = \sigma_{Cr,max} - a_\nabla \frac{\sigma_{Cr,max} - \sigma_{Cr,\infty}}{\sqrt{\text{area}}} \quad (7)$$

Table 1 illustrates the new parameters of the improved DSG criterion, experimentally identified.

2.2 Monte Carlo simulation method

The Monte Carlo simulation (MCS) method is considered as an interesting and a very useful mathematical tool for studying uncertain scenarios and providing statistical and probabilistic analysis. The MCS method is extensively used in engineering disciplines [27, 29–31] to evaluate risk measurements with uncertain parameters, to study the sensitivity effect of the input factor on the desiring response for different dispersions levels, and to compute their reliability.

To compute the reliability, let X be a vector of a random variable in which x_i is an element of this vector, having $f_{X_i}(x_i)$ as a probability density function (PDF). Consider G(x_i), the performance function separating the unsafe and safe zones.

$$G(x_i) = S(x_i) - L(x_i) \quad (8)$$

where $L(x_i)$ and $S(x_i)$ are the load function and the strength function [32], respectively. The probability of failure P_f can be expressed as follows:

$$P_f = \int_{G(x_i<0)} f_{\{X\}}(\{X_i\}) dX_{1 \leq i \leq n} = Pr(L(x_i) > S(x_i)) \quad (9)$$

where Pr and $f_{\{X\}}(\{X_i\})$ represent the probability operator and the joint PDF of the vector X, respectively. Three cases can be

Table 1 Identified parameters of the improved DSG criterion [18]

DSG criterion parameters	Value
β_0	167 (MPa)
α_0	1.8
λ_0	60 (μm)
a_∇	470 (μm)

present: (i) $G(x_i)>0$, (ii) $G(x_i)<0$, and (iii) .. The first and second cases correspond respectively to structural safety and failure conditions. The last case represents the limit state function. Generating N random sampling of $G(\{x\})$, it is assumed that the failure event (i.e., $G(\{x\}) < 0$) extends towards the failure probability P_f when $N \to +\infty$ [33].

$$P_f = \lim_{N\to\infty} \frac{\text{number of failure events}(G(x_i) < 0)}{N} = \lim_{N\to\infty} \frac{1}{N} \sum_{i=1}^{N} I(\{x\}) \tag{10}$$

where $I(\{x\})$ represents the indicator failure function:

$$I(\{x\}) = \begin{cases} 1 & \text{if } G(\{x\}) < 0 \\ 0 & \text{if } G(\{x\}) \geq 0 \end{cases} \tag{11}$$

Finally, the reliability R is computed as follows:

$$R = 1 - P_f \tag{12}$$

2.3 Short review of the response surface method (RSM)

The response surface method (RSM) is an empirical approach proposed at first by Bucher and Bourgund [34] and improved later by Rajashekhar and Ellingwood [35]. It consists in establishing simple relationships between diverse process parameters and their responses with diverse chosen criteria. RSM searches the signification of these parameters on the associated responses [36]. In fact,

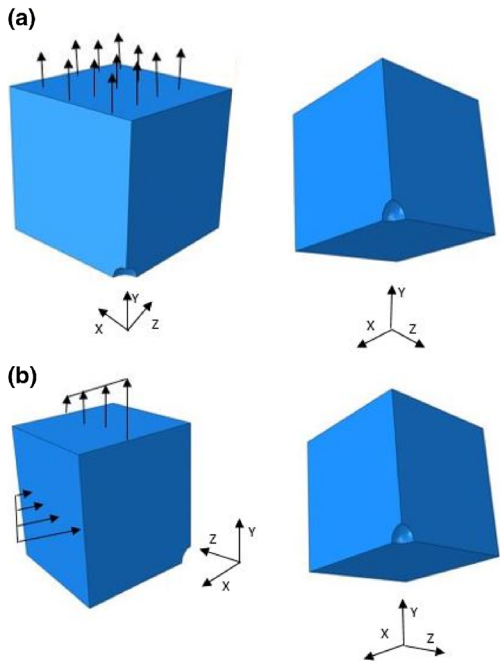

Fig. 2 Finite element model: load and boundary conditions: **a** tension loading, **b** torsion loading

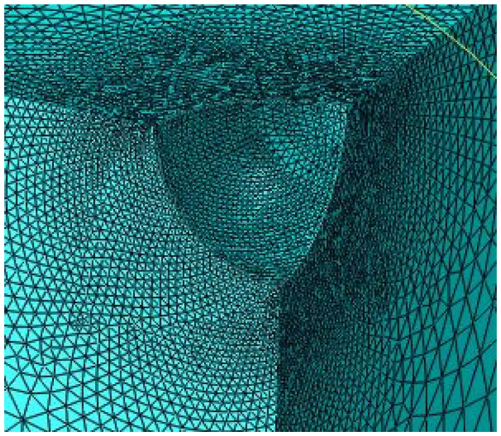

Fig. 3 Mesh refinement around the defect

RMD is an easy and efficient way to build empirical models and to optimize various industry products. Since their first use, many of the improvements have been introduced to RSM [37] but the principle steps of this approach that are often employed can be summed up as follows:

(i) Preparing the experimental design
(ii) Generating the obtained design using MINTAB software
(iii) Plotting the surface response curves
(iv) Determining the analytical model representing the relationship between the various input factors and their responses
(v) Performing additional tests to validate the developed model

This approach gives often a simple relation between the output responses and their input factors. This relationship may be represented as

$$Y = f(X_1, X_2, X_3 \ldots\ldots\ldots X_n) \pm \varepsilon \tag{13}$$

where Y represents the designed response, f represents the response surface, $X_{i\in[1,n]}$ represents the independent inputs, and ε is the error.

In this work, the RSM will be adopted to qualify the interactions between the inputs (SDAS and defect size) and the output (fatigue limit). Therefore, fatigue limit with the corresponding SDAS and defect size is fulfilled to build the response surface.

Table 2 A356-T6 mechanical properties and cyclic fatigue parameters

Material	E (GPa)	ν	R_0 (MPa)	Q	b	C	D
A356-T6	72	0.33	200	30	10	58,000	680

Table 3 Design matrix under fully reserved tension fatigue loading for $\sqrt{area} \leq 500$

Order	$\sqrt{area}$ (μm)	SDAS (μm)	σ_D (MPa)
1	0	39.5	91
2	0	55.75	85
3	0	72	77
4	250	39.5	91
5	250	55.75	85
6	250	72	77
7	500	39.5	91
8	500	55.75	78
9	500	72	67

Table 5 Design matrix under fully reserved torsion fatigue loading for $\sqrt{area} \geq 500$

Order	$\sqrt{area}$ (μm)	SDAS (μm)	σ_D (MPa)
1	0	39.5	88
2	0	55.75	62
3	0	72	50
4	250	39.5	88
5	250	55.75	62
6	250	72	50
7	500	39.5	80
8	500	55.75	60
9	500	72	48

Fatigue limit will be described by a second-order polynomial known as the quadratic model which is expressed by the following relationship:

$$f = a_0 + \sum_{i=1}^{n} a_i X_i + \sum_{i=1}^{n} a_{ii} X_i^2 + \sum_{i<j}^{n} a_{ij} X_i X_j + \varepsilon \qquad (14)$$

where $a_i, a_{ii,}$ and a_{ij} are the coefficients of the linear effect, quadratic effect, and the interaction between xi and xj, respectively.

3 Stress distribution around the defect

A three-dimensional finite element (FE) analysis using ABAQUS software is implemented to characterize fatigue response of defective A356-T6 aluminum material.

The three-dimensional REV model employed to describe the stress distribution around the surface pore is a cube containing a spherical defect. Owing to the symmetry of the problem, only a quarter of the specimen is modeled. Symmetry and boundary conditions are implemented as illustrated in Fig. 2. The cube is meshed by mean of four node linear tetrahedral solid elements C3D4 (Fig. 3). Around the defect, a very fine mesh is adopted due to the high strain and stress gradients.

Due to FE simulations, the highest stressed regions near the defect were localized. In the FE analysis, the Chaboche kinematic hardening model is used to characterize the material response during cyclic loading. This plasticity model is able to take into account the mean stress relaxation, Baushinger effect, and cyclic hardening.

The main mechanical proprieties for this alloy are Young modulus E = 70 GPa, Poisson's ratio = 0.3, yield stress $R_{p0.2\ \%}$ = 200 MPa, ultimate tensile strength R_m = 317 MPa, and elongation to failure A = 16 %. Table 2 summarizes the cyclic fatigue parameters for the concerned material [38].

Table 4 Design matrix under fully reserved tension fatigue loading for $\sqrt{area} \geq 500$

Order	$\sqrt{area}$ (μm)	SDAS (μm)	σ_D (MPa)
1	500	39.5	91
2	500	55.75	78
3	500	72	67
4	700	39.5	74
5	700	55.75	64
6	700	72	59
7	900	39.5	64
8	900	55.75	59.5
9	900	72	56

Table 6 Design matrix under fully reserved torsion fatigue loading for $\sqrt{area} \geq 500$

Order	$\sqrt{area}$ (μm)	SDAS (μm)	σ_D (MPa)
1	500	39.5	80
2	500	55.75	60
3	500	72	48
4	700	39.5	57
5	700	55.75	52
6	700	72	44
7	900	39.5	49
8	900	55.75	46
9	900	72	41

4 Applications

4.1 Application 1: finite element analysis

In this section, 3D finite element calculations are carried out for different cases of defect sizes and loadings near the fatigue limit to determine stress distribution. Experimental results showed that cracks initiate and occur always in the shear plane which is the highest loaded plane (HLP) [39–42]. This HLP is perpendicular to the maximum stress direction. In the present study, Crossland equivalent stress (σ_{eq}^{Cr}) evolution will be studied in the HLP. FE simulations of σ_{eq}^{Cr} for both cases: tension and torsion loading showed that

- For an arc centered on the defect, σ_{eq}^{Cr} is almost constant with a scattering which does not exceed 2 %.
- In the HIP, σ_{eq}^{Cr} distribution depends only of the $\frac{r}{R}$ ratio, the applied load, and the SDAS value.
- In the case of alternate tension load, σ_{eq}^{Cr} can be interpolated by the following expression:

$$\sigma_{eq}^{Cr} = \frac{\tau_{-1}}{\sigma_{-1}}\sigma_a \left(\frac{1}{\left(\frac{r}{R}\right)^4} + 1\right) \tag{15}$$

- In the case of alternate torsion load, σ_{eq}^{Cr} can be interpolated by the following expression:

$$\sigma_{eq}^{Cr} = \frac{\tau_{-1}}{\sigma_{-1}}\sigma_a \left(\frac{1}{\left(\frac{r}{R}\right)^5} + 1\right) \tag{16}$$

- σ_{-1} and τ_{-1} are expressed, for the A356-T6 alloy, as a function of λ_2 as follows [18]:

$$\sigma_{-1}\left(\lambda_2\right) = \frac{3\beta_0 \exp\left(-\frac{\lambda_2}{\lambda_0}\right)}{\lambda_0 \exp\left(-\frac{\lambda_2}{\lambda_0}\right) + \sqrt{3}} \tag{17}$$

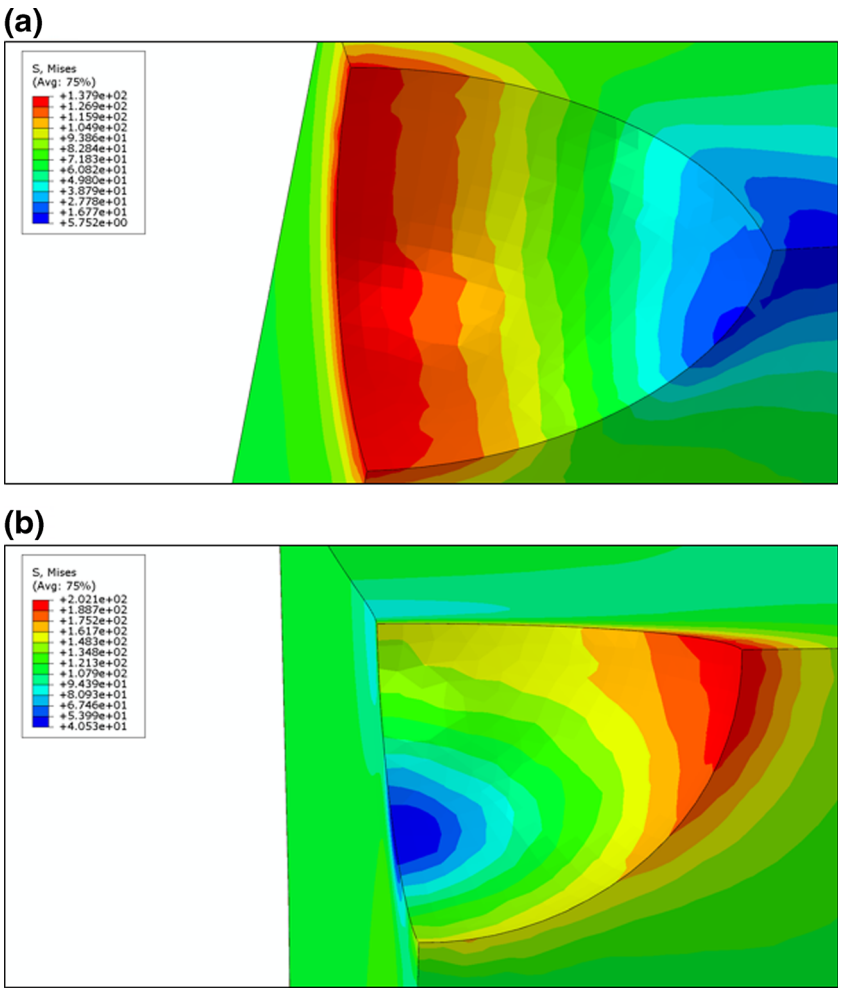

Fig. 4 Von Mises equivalent stress around the defect: **a** alternate tension loading $\sigma_a = 70$ MPa,**b** alternate torsion loading $\tau_a = 70$ MPa

$$\tau_{-1}\ (\lambda_2) = \beta_0 \exp\left(-\frac{\lambda_2}{\lambda_0}\right) \tag{18}$$

where τ_{-1}, σ_{-1}, σ_a, R, r, λ_0, and λ_2 are the defect-free fatigue limit under fully reserved torsion loading, defect-free fatigue limit under fully reserved tension loading, the applied load, the defect radius, the distance from the defect center to the considered point, parameter experimentally identified, and the SDAS parameter, respectively.

4.2 Application 2: HCF reliability computation

Fatigue tests in A356-T6 show a large dispersion in predicting the endurance limit; this dispersion is mainly attributed to the microstructure (SDAS). In fact, scattered results are detected on the Kitagawa diagrams under fully reserved tension and torsion loading especially for a defect size under 400 ∓ 100 μm [18, 20–23]. In this zone, the HCF behavior of A356-T6 is mainly affected by the microstructure SDAS which is the origin of fatigue failure. A significant fatigue data scattering was observed especially under torsion fatigue loading [18]. A deterministic Kitagawa diagram seems to be unable to estimate A356-T6 fatigue response due to the SDAS dispersion which confirms the need to study the probabilistic effect of this parameter for predicting the fatigue limit under both tension/torsion loading.

In this section, a probabilistic approach for predicting fatigue limit of A356-T6 is implemented. The main

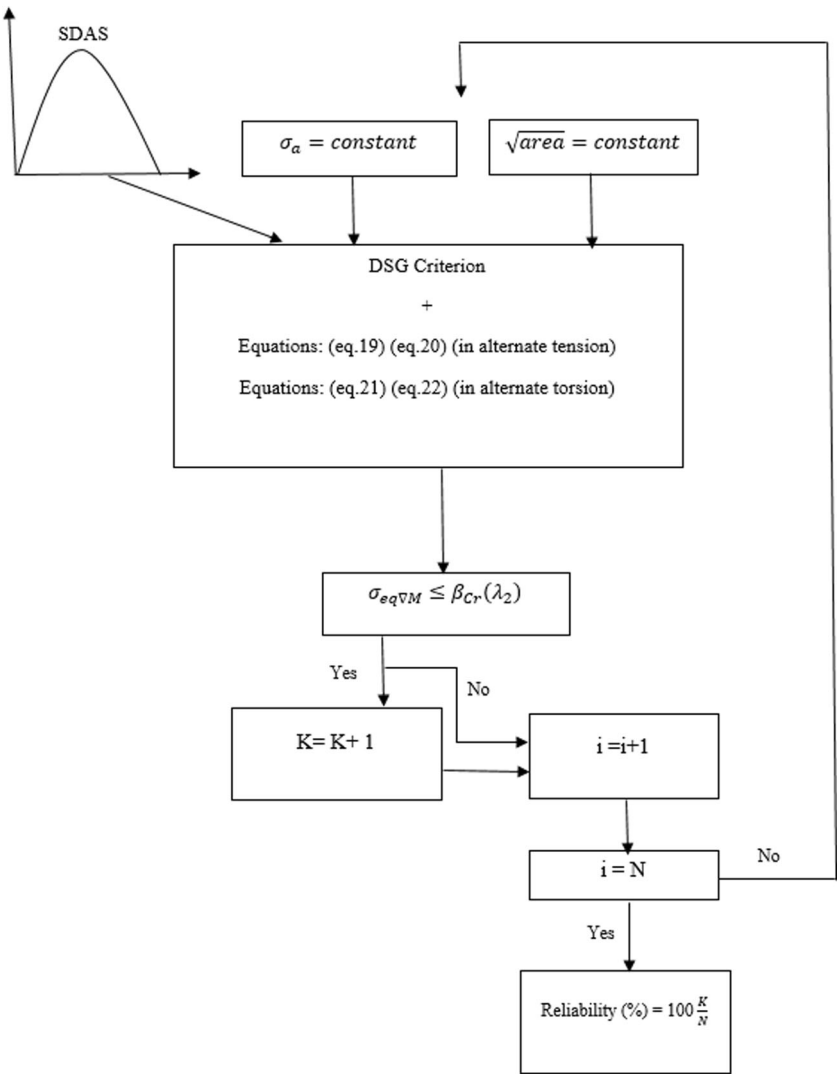

Fig. 5 Flowchart proposed to compute reliability

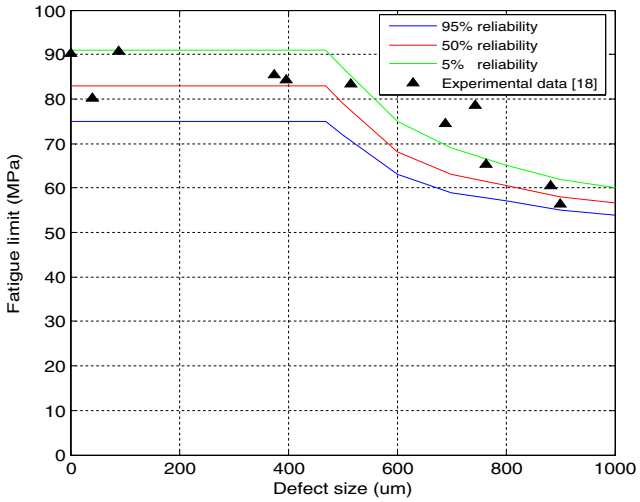

Fig. 6 Iso-probabilistic Kitagawa diagram under fully reserved tension fatigue loading

procedure for developing the probabilistic model using FE analysis and Monte Carlo simulation method is summarized as follows:

(i) An elastic-plastic analysis using the nonlinear isotropic/kinematic hardening model embedded in ABAQUS is carried out. The distribution of Crossland equivalent stress (σ_{eq}^{Cr}) in the HLP is determined in the case of fully reserved tension and torsion loading. It is verified that σ_{eq}^{Cr} can be interpolated, by mathematical expressions depending on the applied load, SDAS, and ($\frac{r}{R}$) ratio as mentioned in application 1.

(ii) The new expressions Eq. 15 and Eq. 16 are inserted in the DSG criterion instead of the analytical expressions of σ_{eq}^{Cr} to predict fatigue limits for each case of loading where

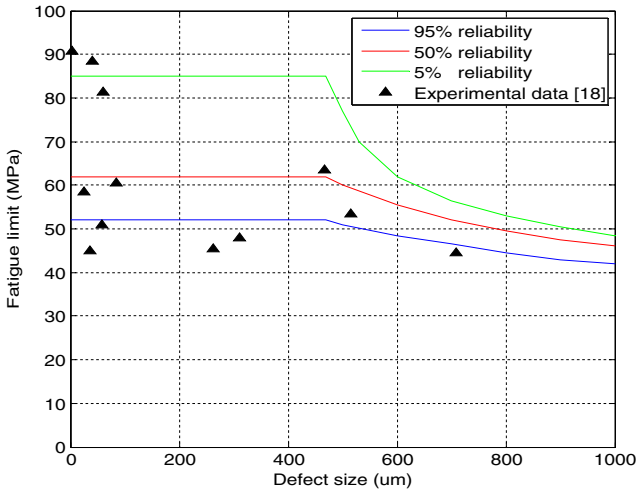

Fig. 7 Iso-probabilistic Kitagawa diagram under fully reserved torsion fatigue loading

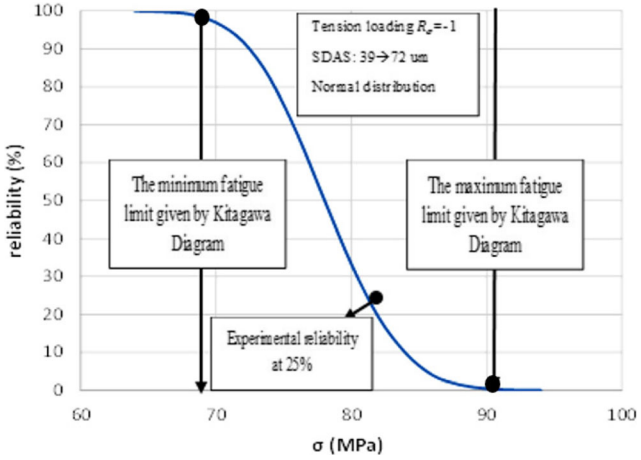

Fig. 8 Prediction of the HCF reliability under fully reserved tension loading for $\sqrt{area}$ = 500 μm

– In the case of fully reserved tension:

$$\sigma_{Cr,mMax} = \frac{\tau_{-1}(\lambda_2)}{\sigma_{-1}(\lambda_2)}\sigma_a\left(\frac{1}{\left(\frac{R}{R}\right)^4}+1\right) \tag{19}$$

$$\sigma_{Cr,\infty} = \frac{\tau_{-1}(\lambda_2)}{\sigma_{-1}(\lambda_2)}\sigma_a\left(\frac{1}{\left(\frac{\sqrt{area}}{R}\right)^4}+1\right) \tag{20}$$

– In the case of fully reserved torsion:

$$\sigma_{Cr,Mmax} = \frac{\tau_{-1}(\lambda_2)}{\sigma_{-1}(\lambda_2)}\sigma_a\left(\frac{1}{\left(\frac{R}{R}\right)^5}+1\right) \tag{21}$$

$$\sigma_{Cr,\infty} = \frac{\tau_{-1}(\lambda_2)}{\sigma_{-1}(\lambda_2)}\sigma_a\left(\frac{1}{\left(\frac{\sqrt{area}}{R}\right)^5}+1\right) \tag{22}$$

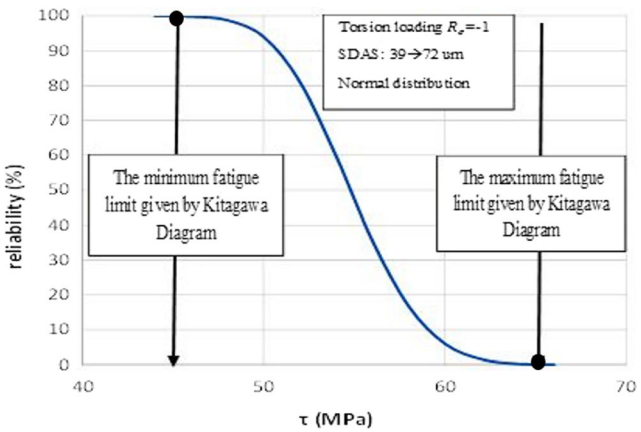

Fig. 9 Prediction of the HCF reliability under fully reserved torsion loading for $\sqrt{area}$ = 600 μm

(iii) The experimental investigations of Iben Houriya et al. [18] have been made in a range of microstructure (SDAS) betwee36 umn 36 an 72 umd 72 μm. Several researches [18, 20, 21] showed that the critical defect size affecting the fatigue response of A356-T6 is $\sqrt{area} = 400 \overline{+} 100$ μum; below this value, this alloy is considered as a defect-free material. The probabilistic approach is carried out by taking into account the SDAS dispersions which are assumed to be normally distributed [18, 23]. The average SDAS is 52 μm, with a standard deviation equal to 5 μm.

(iv) The "strength-load" method coupled with Monte Carlo simulations is used to compute fatigue reliability. It is observed that when the standard deviation of the computed reliabilities decreases, the Monte Carlo number (N) increases. The value of the relative reliability becomes almost constant for a Monte Carlo number higher than 10^4. Therefore, the choice of N equal to 10^4 is justified.

(v) The generation of random sampling of the SDAS value leading to transform the Kitagawa diagram into three zones: (i) an uncertainty zone, (ii) a zone of absolute failure, and (iii) a zone of absolute safety.

(vi) The reliability-fatigue limit curves are plotted for different defect sizes.

(vii) The iso-probabilistic Kitagawa diagrams (PKDs) are determined for 5, 50, and 95 % reliabilities under fully reserved tension/torsion loading.

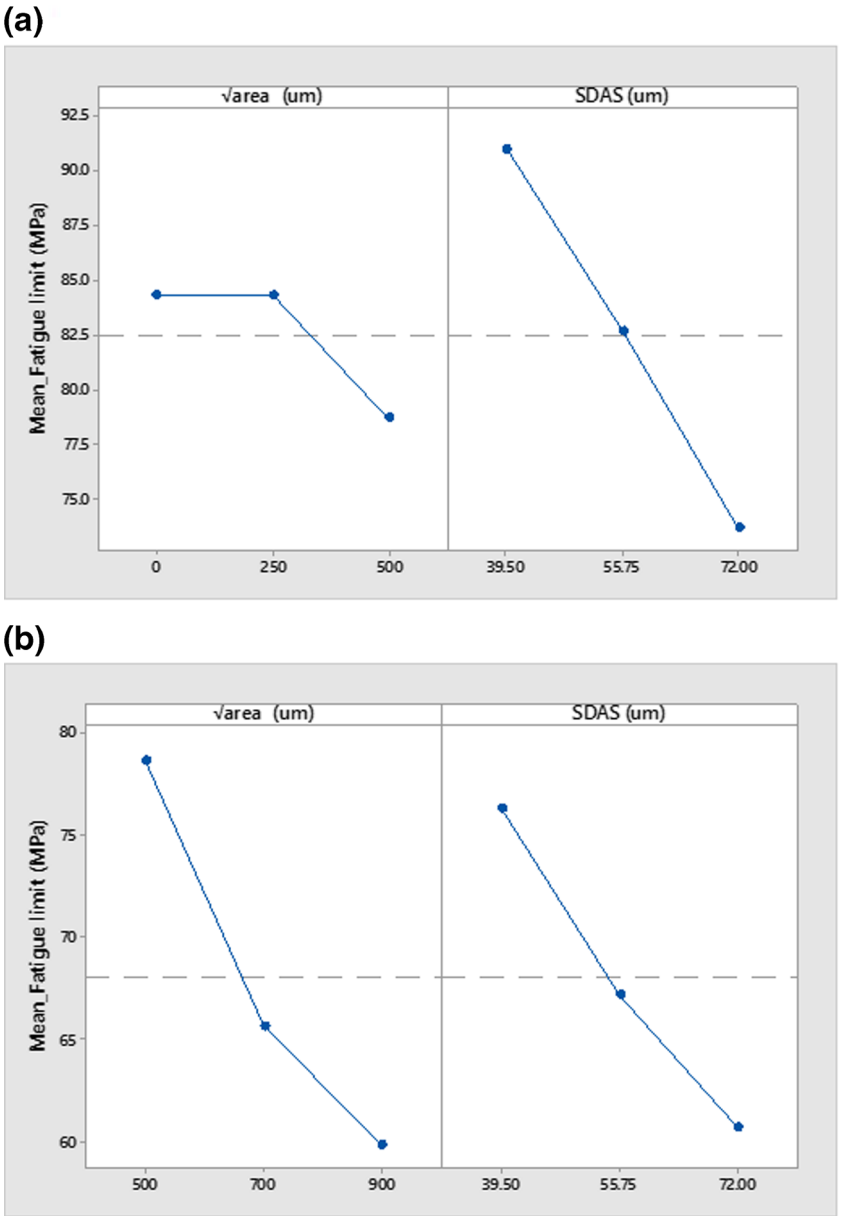

Fig. 10 Main effects plot on the fatigue limit under tension fatigue loading: **a** for $\sqrt{area} \leq 500$ and **b** for $\sqrt{area} \geq 500$

4.3 Application 3: design of experiment

In this section, experiments were designed based on numerical simulations carried out on A356-T6 aluminum alloy.

The aim of the design matrix (DM) consists in extracting relationships and interactions between the response (the fatigue limits under fully reserved tensile and torsion loading) and different input parameters (defect size and SDAS).

In fact, this method allows investigating both the individual effects of each parameter and describing the interactions between them. The ED generates nine experiments with three levels, in each case. The obtained results are analyzed using MINITAB 17.0 software. Defect size and SDAS are chosen as the main independent input parameters, and the fatigue limit is considered as an output response (Tables 3, 4, 5, and 6).

5 Discussion

(i) In the first application, numerical simulations are carried out under fully reserved tension/torsion loading to validate Eqs. 15 and 16. Figure 4 shows the stress distribution around a spherical defect in the case of each loading. A comparison between the computed σ_{eq}^{Cr} using finite element analysis and the Eq. 15 and Eq. 16 under different conditions (SDAS, loading, and $\sqrt{area}$) are realized. The obtained results prove the validity of this interpolation (error < 5 %).

(ii) In the second application, a probabilistic approach is proposed to compute the Kitagawa diagram by taking into account the SDAS dispersion. The Monte Carlo method combined with the DSG criterion (using the interpolated expressions of σ_{eq}^{Cr}) is implemented to

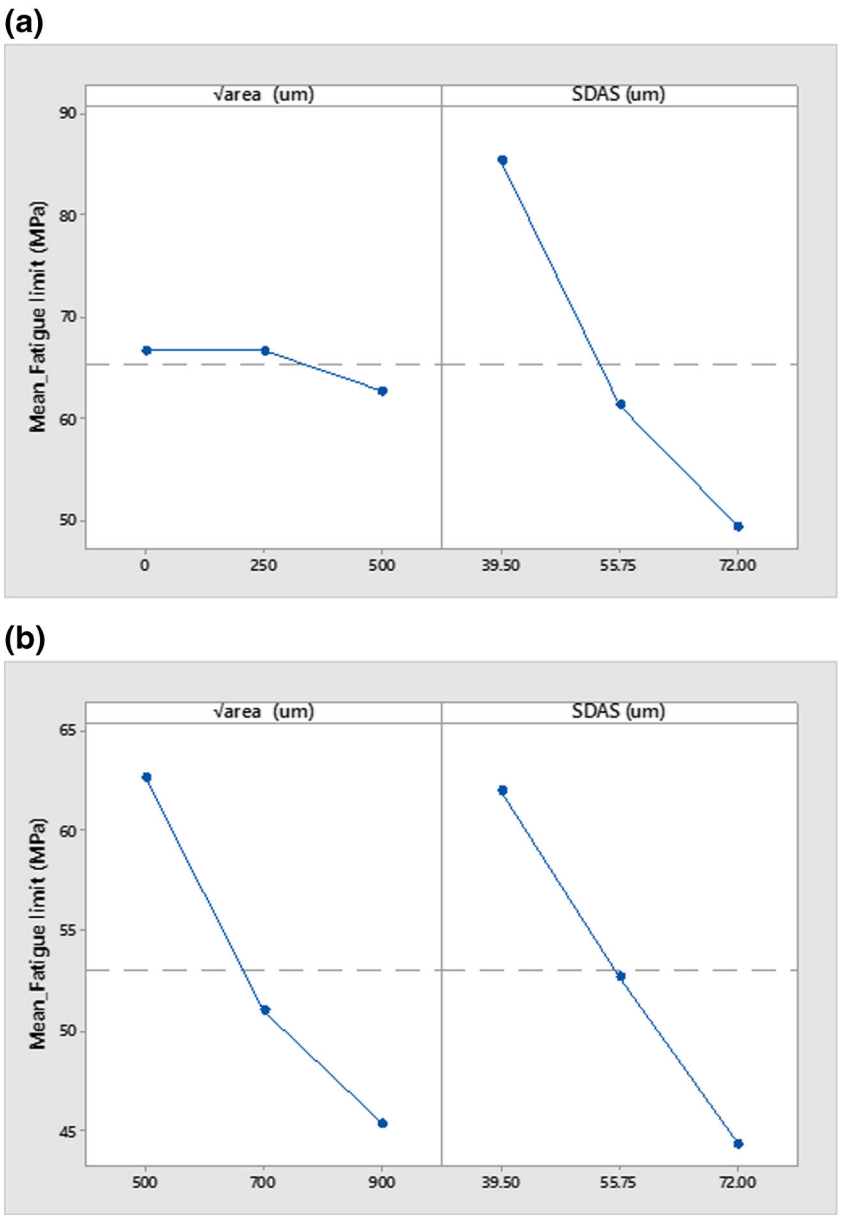

Fig. 11 Main effects plot on the fatigue limit under torsion fatigue loading: **a** for $\sqrt{area} \leq 500$ and **b** for $\sqrt{area} \geq 500$

calculate reliability. Figure 5 shows the method used to calculate the reliability.

(iii) Figures 6 and 7 show the obtained iso-probabilistic Kitagawa diagram (PKD) for 5, 50, and 95 % reliabilities under both fully reserved tension/torsion loading. It is observed that these results are in good agreement with experimental data [18]. It is noted that the security zone is reduced when the reliability values increase.

(iv) In both cases of alternate tension and alternate torsion, it is worth observing that, for the same level of applied stress amplitude, the reliability decreases when the SDAS value increases and vice versa. This observation is physically coherent with the previous experimental result. Moreover, it should be noted that the decrease of the reliability is more important in the case of alternate torsion than in the case of alternate tension.

(v) In the case of fully reserved tension loading (Fig. 6), it is noted that the fatigue limit response is normally distributed. It also is observed that the probabilistic results converge for big defect sizes. This result is consistent with experimental observations [18].

(vi) In the case of fully reserved torsion loading (Fig. 7), it is noted that fatigue limit response is log-normally distributed for a range of defect sizes under than 500 μm and, for bigger defects, it becomes normally distributed. On the basis of these results, it can be retained that the alternate torsion is more sensitive to the SDAS scattering than the alternate tension especially for small defects (≤500). These observations are coherent with previous experimental investigations [18]. These P-K-D allow the engineer to be engaged in a practical problem to evaluate the fatigue limit in a more efficient and safe way.

(vii) Figures 8 and 9 show the change of the reliability value with the applied stress for a defect size equal to 500 μm in the case of alternate tension and for a defect size equal to 600 μm in the case of alternate torsion. In Fig. 8, a deterministic fatigue limit, taken from experimental data [18] and corresponding to defect specimens equal to 500 μm, is compared with reliability results. It is well noticed that this loading point corresponds to a reliability of 25 % which seems to be reasonable.

(viii) Figure 10 shows the main effects of SDAS and defect size ($\sqrt{area}$) on the fatigue limit under tension loading for $\sqrt{area} \leq 500$ and $\sqrt{area} \geq 500$ μm. It is noted that for $\sqrt{area} \leq 500$ μm, defect size has not an important effect on the fatigue limit. However, it is observed that SDAS has a linear effect which proves that the fatigue response is strongly depending on the SDAS value. For $\sqrt{area} \geq 500$, defect size's effect becomes more

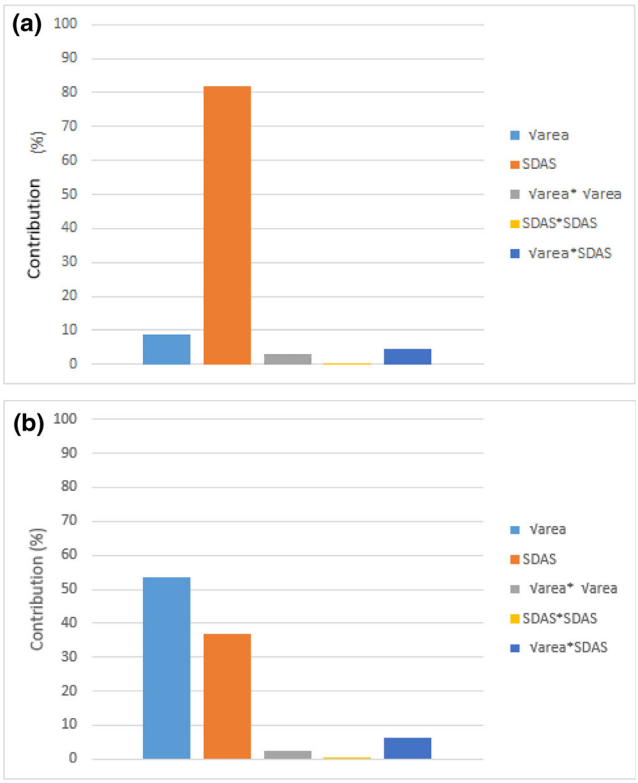

Fig. 12 Pareto diagram: linear, square, and way interaction contribution of SDAS and $\sqrt{area}$ on the fatigue limit under fully reserved tension fatigue loading: **a** for $\sqrt{area} \leq 500$, **b** for $\sqrt{area} \geq 500$

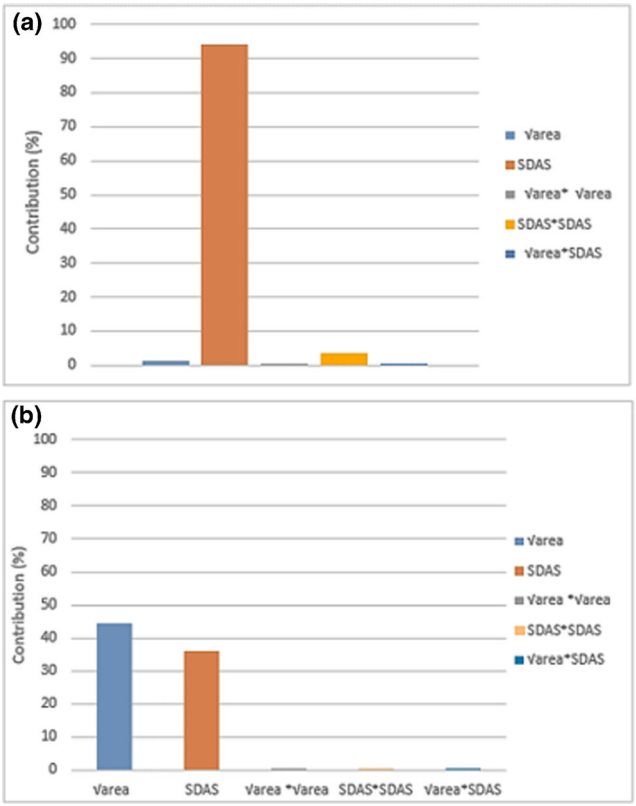

Fig. 13 Pareto diagram: linear, square, and way interaction contribution of SDAS and $\sqrt{area}$ on the fatigue limit under fully reserved torsion fatigue loading: **a** for $\sqrt{area} \leq 500$, **b** for $\sqrt{area} \geq 500$

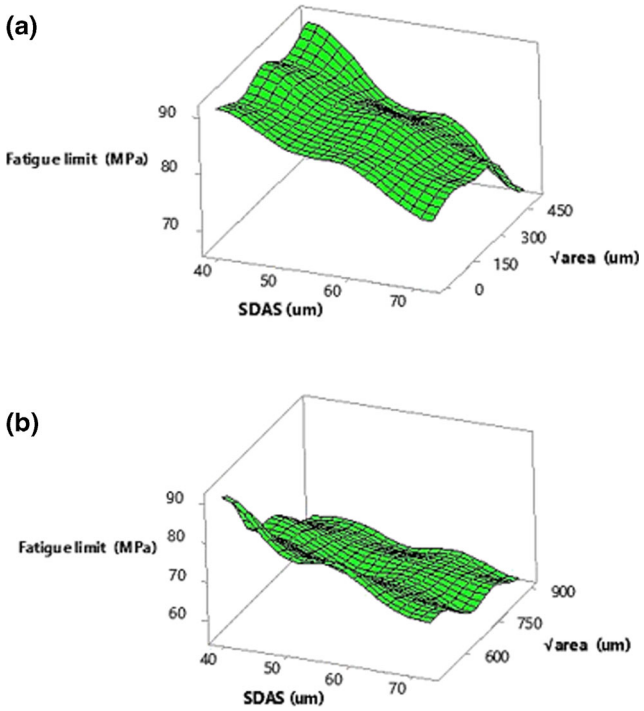

Fig. 14 Response surface diagrams alternate tension. **a** $\sqrt{area}\leq 500$, **b** $\sqrt{area}\geq 500$

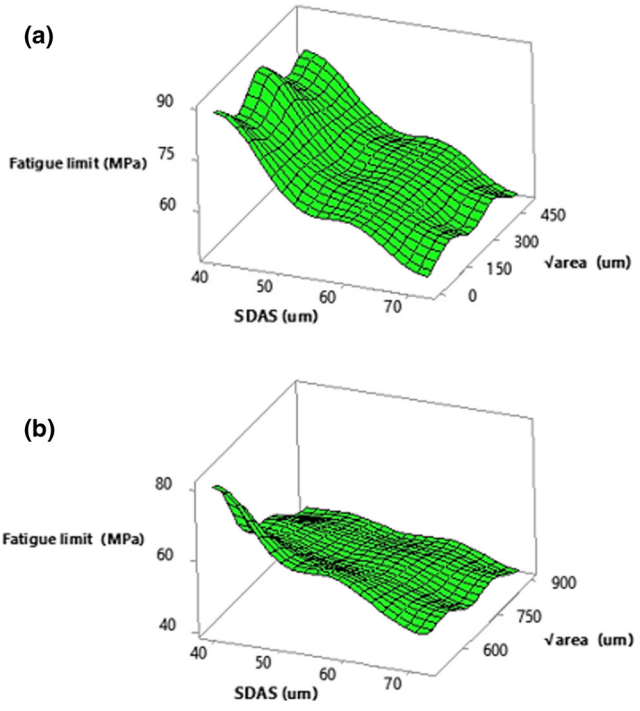

Fig. 15 Response surface diagrams alternate torsion **a** $\sqrt{area}\leq 500$, **b** $\sqrt{area}\geq 500$

significant and fatigue limit depends in this case on both parameters (defect size and SDAS).

(ix) Figure 11 shows the main effects of SDAS and defect size ($\sqrt{area}$) on the fatigue limit under torsion loading for $\sqrt{area}\leq 500$ and $\sqrt{area}\geq 500$ μum. It is noted that for $\sqrt{area}\leq 500$ μum, defect size has practically no effects on the fatigue limit. However, the impact of the SDAS parameter becomes more significant compared to the case of tension loading (Fig. 10a).

For $\sqrt{area}\geq 500$, as it was shown in the case of alternate tension (Fig. 11b), fatigue response, under torsion loading, is governed by both the defect size and the SDAS.

(x) Figures 12 and 13 represent the Pareto diagrams in the case of fully reserved tension and alternate torsion, respectively. It is noted that there is no interaction between the input parameters in both cases of loading. Moreover, these diagrams show that, for small defects, fatigue response is mainly governed by SDAS and for big defects it becomes governed by SDAS and defect size.

(xi) Figures 14 and 15 present the surface response curves of endurance limit as a function defect size and SDAS under fully reserved tension/torsion loading. From Figs. 14a and 15a, it is observed that for a given SDAS value, fatigue response is barely changed in term of $\sqrt{area}$ regardless of the applied load. However, for $\sqrt{area}\geq 500$ (Fig. 15b), the fatigue response decreases when $\sqrt{area}$ and SDAS increase. In fact, for a given SDAS value, fatigue limit is strongly affected by the increase of size defect.

6 Conclusions

The aim of this paper is to propose a reliability approach which takes into account the dispersion in casting aluminum alloy. From this work, it can be concluded that:

(i) HCF response of A356-T6 alloy shows a large dispersion that is mainly attributed to SDAS dispersion.

(ii) The reliability is computed by coupling of FE analysis, defect stress gradient (DSG) criterion, and Monte Carlo simulation (MCS) method. A good agreement was found between simulations and experimental data in the case of fully reserved tension and torsion loadings.

(iii) Using the proposed approach, it was shown that the reliability is very sensitive to the SDAS value, especially for small defect sizes.

(iv) The dispersion of the Kitagawa diagram due to the SDAS scattering decreases for big defect sizes.

(v) The iso-probabilistic Kitagawa diagram corresponding to 5, 50, and 95 % fatigue reliability under fully reserved

tension and torsion loadings has been performed. This method allows engineers to be engaged in practical problems for predicting fatigue limit in a more efficient and reliable way.

(vi) The suggested approach results in improving the deterministic fatigue limit prediction by considering the dispersions of the fatigue material data especially the SDAS parameter.

References

1. Wang QG, Caceres CH, Griffiths JR (2003) Damage by eutectic particle cracking in aluminum casting alloys A356/A357. Metallurgical and material transactions A 34A:2901
2. J.B. Jordon, M.F Horstemeyer, N. Yang, J.F. Major, K.A. Gall, J. Fan, D.L. McDowell. Microstructure inclusion influence on fatigue of a cast A356 aluminum alloy; 2010, 41A: 356.
3. Wang QG, Praud M, Needleman A, Kim KS, Griffiths JR, Davidson CJ, Caceres CH, Benzarga AA (2010) Size effects in aluminum alloy castings. Acta Mater 58:3006–3013
4. McDowell DL (2007) Simulation-based strategies for microstructure-sensitive fatigue modelling. Mater Sci Eng A 468-470
5. Borbély A, Mughrabi H, Eisenmeier G, Hoppel HW (2002) A finite element modelling study of strain localization in the vicinity of near surface cavities as a cause of subsurface fatigue crack initiation. Int J Fract 115:227–232
6. Ceschini L, Morri AL, Morri AN (2014) Estimation of local fatigue behaviour in A356-T6 gravity die cast engine head based on solidification defects content. International Journal of Cast Metals Research 27:1
7. Shaha SK, Czerwinski F, Kasprzak W, Friedman J, Chen DL (2015) Microstructure and mechanical properties of AL-Si cast alloy with additions of Zr-V-Ti. Material & Design 83:801–812
8. Gonzales R, Gonzales A, Talamantes-Silva J, Valtierra S, Mercado-Solis RD, Garza NF, Montes-de-Oca RC (2013) Fatigue of an aluminium cast alloy used in the manufacture of automotive engine blocks. Int J Fatigue 54:118–126
9. Ammar HR, Samuel AM, Samuel FH (2008) Porosity and the fatigue behavior of hypoeutectic and hypereutectic aluminum-silicon casting alloys. Int J Fatigue 30:1024–1035
10. Le V-D, Morel F, Bellett D, Saintier N, Osmond P (2016) Multiaxial high cycle fatigue damage mechanisms associated with the different microstructural heterogeneities of cast aluminum alloys. Material Science & Engineering A 649:426–440
11. Ran G, Zhou JE (2007) Metallographic characterization of porosity in a cast aluminum alloy A356-T6. Mater Sci 546:989–994
12. Xu Z, Wen W, Zhai T (2012) Effects of pore position in depth on stress/strain concentration and fatigue crack initiation. Metall Mater Trans A 43:2763. doi:10.1007/s11661-011-0947-x
13. Davidson CJ, Griffiths JR, Badiali M, Zanada A (2000) Fatigue properties of a semi-solid cast AL-7Si-0.3Mg-T6 alloy. Metallurgical Science and Technology 18:2
14. Ammar HR, Samuel AM, Samuel FH (2008) Effect of casting imperfections on the fatigue life of 319-F and A356-T6 Al-Si casting alloys. Material Science & Engineering A 473:65–75
15. Wang QG, Apelian D, Lados DA (2001) Fatigue behavior of A356-T6 aluminium cast alloys. Part I. Effect of casting defects. Journal of Light Metal 1:73–84
16. Wang QG, Apelian D, Lados DA (2001) Fatigue behavior of A356-T6 aluminium cast alloys. Part II. Effect of microstructural constituents. Journal of Light Metal 1:85–97
17. Li P, Lee PD, Maijer DM, Lindley TC (2009) Quantification of the interaction within defect populations on fatigue behavior in an aluminum alloy. Acta Mater 57:3539–3548
18. IbenHouriya M, Nadot Y, Fathallah R, Roy M, Maijer DM (2015) Influence of casting defect and SDAS on the multiaxial fatigue behaviour of A356-T6 alloy including mean stress effect. Int J Fatigue 80:90–102
19. Murakami Y (2002) Metal fatigue: effects of small defects and nonmetallic inclusions. Elsevier Editor, New York
20. Roy MJ, Nadot Y, Nadot-Martin C, Bardin P-G, Maijer DM (2011) Multiaxial Kitagawa analysis of A356-T6. Int J Fatigue 33:823–832
21. Roy M, Yves N, Maijer DM, Benoit G (2012) Multiaxial fatigue behaviour of A356-T6. Fatigue & Fracture of Engineering Materials & Structures 35:1148–1159
22. Koutiri I, Bellett D, Morel F, Augustins L, Adrien J (2013) High cycle fatigue damage mechanisms in cast aluminum subject to complex loads. Int J Fatigue 47:44–57
23. Mu P, Nadot Y, Nadot Martin C, Chabod A, Serrano-Munoz I, Verdu C (2014) Influence of casting defects on the fatigue behavior of cast aluminum AS7G06-T6. Int J Fatigue 63:97–109
24. Mu P, Nadot Y, Serrano-Munoz I, Chabod A (2014) Influence of complex defect on cast AS7G06-T6 under multiaxial fatigue loading. Eng Fract Mech 123:148–162
25. Rice JR (1988) Elastic fracture mechanics concept for interfacial cracks. J Appl Mech 55:99
26. Susmel L, Taylor D (2008) The theory of critical distances to predict static strength of notched brittle components subjected to mixed-mode loading. Eng Fract Mech 75:534–550
27. Bouraoui C, Ben Sghaier R, Fathallah R (2009) An engineering predictive design approach of high cycle fatigue reliability of shotpeened metallic parts. Mater Des 30:475–486
28. Gadouini H, Nadot Y, Rebours C (2008) Influence of mean stress on the multiaxial fatigue behaviour of defective materials. Int J Fatigue 30:1623–1633
29. Nasr A, Bouraoui C, Fathallah R, Nadot Y (2009) Probabilistic high cycle fatigue behaviour of nodular cast iron containing casting defects. Fatigue & Fracture of Engineering Materials & Structures 32: 292–309
30. He W, Liu J, Xie D (2015) Probabilistic life assessment on fatigue crack growth in mixed-mode by coupling of Kriging model and finite element analysis. Eng Fract Mech 139:56–77
31. Sanches RF, de Jesus AMP, Correia JAFO, da Silva ALL, Fernandes AA (2015) A probabilistic fatigue approach for riveted joints using Monte Carlo simulation. J Constr Steel Res 110:149–162
32. Zhao YG, Ono T (2001) Moment methods for structural reliability. Struct Safety 23(1):47–75
33. Ditlevsen O, Madsen HO (1996) Structural reliability methods. Wiley, Hoboken
34. Bucher CG, Bourgund U (1990) A fast and efficient response surface approach for structurel reliability problems. Struct Saf 7(1):57–66
35. Rajashekhar MR, Ellingwood BR (1990) A now look at the response surface approach for reliability analysis. Struct Saf 12(3): 205–220
36. Myers RH, Mongomery DH (1995) Response surface methodology. Wiley, USA
37. Faravelli L (1989) Response-surface approach for reliability analysis. Journal Engineering Mechanics 115(12):2763–2781
38. Le Pen E, Baptiste D (2001) Prediction of the fatigue-damaged behaviour of Al/Al_2O_3 composites by a micro-macro approach. Compos Sci Technol 61:2317–2326

39. Nadot Y, Billaudeau T (2006) Multiaxial fatigue limit criterion for defective materials. Eng Fract Mech 73:112–133
40. Ting J, Lawrence FV (1993) Modelling the long-life fatigue behaviour of a cast aluminium alloy. Fatigue Fract Eng Mater Struct 1993(16):631–647
41. Wannes H, Nasr A, Bouraoui C (2016) New fatigue limit assessment approach of defective material under fully reserved tension and torsion loading. Mechanic & Industry 113:310
42. Vincent M, Nadot-Martin C, Nadot Y, Dragon A (2014) Fatigue from defect under multiaxial loading: defect stress gradient (DSG) approach using ellipsoidal equivalent inclusion method. Int J Fatigue 59:176–187